A standard model for the investigation of aerodynamic and aerothermal loads on a re-usable launch vehicle

Tamas Bykerk *
* *German Aerospace Center (DLR)*
Bunsenstrasse 10, Goettingen, 37073
tamas.bykerk@dlr.de

Abstract

This paper presents a generic geometry for the study of aerodynamic and aerothermal behaviour relevant to re-usable launchers. The model, denoted RFZ, can be broken down into three subcategories for ascent, re-entry and landing. The vehicle design is presented, outlining simplifications made to retain key features of the vehicle while ensuring a manufacturable and meshable geometry. Computational studies have been performed at a trajectory point reflecting the start of the aerodynamic glide phase for a down-range landing scenario. Results present a trim analysis for two fin deflection settings at three different angles of attack. Additional investigations have been performed analysing the internal flow conditions of the first stage nozzle. Initial calculations suggest that the vehicle is trimmable at the trajectory point investigated. These are the first of many test cases which will look to address common questions with these types of vehicles, including but not limited to, surface heating through retro-propulsion and aerodynamic glide phases, plume-plume and plume-structure interactions, as well as vehicle stability and control. The geometry and results will be made openly available to the research community to promote collaboration in understanding the design challenges associated with re-usable launchers.

1. Introduction

Aeronautical engineers have a long history of developing standardized models for wind tunnel calibrations and data comparisons between facilities. They are extremely useful in providing baseline datasets for correlation of results, data repeatability over time and verifying model installation or data acquisition systems. Reference models are also particularly relevant from the perspective of numerical analyses, where different codes can be directly compared with each other or assumptions and solver settings can be experimented with to determine solution sensitivity to certain parameters. A standardized reference model typically fulfills two main criteria. Firstly, they are simplistic in shape with a precisely defined geometry and secondly, they are representative of realistic configurations to ensure that the results are relevant. Examples of existing standard models include the AGARD-B[1], ONERA-M[2] and the Standard Dynamics Model (SDM)[3], which have been circulating for decades. Recently, models such as the NASA CRM[4] and the SSAM-Gen5[5] provide more up to date and relevant aircraft geometries from the past 10 to 20 years.

While aeronautical engineers are well covered with standard aircraft models, the space community is not. Given the sudden and urgent interest in re-usable spacecraft over the past decade, a reference model which serves the research community in facilitating validation of numerical techniques in the generation of aerodynamic and aerothermal data over the entire trajectory is lacking. The purpose of this paper is to introduce a re-usable launch vehicle (RLV) geometry where computational models and results will be made openly available to the research community. It is envisioned that this model will serve as a consistent validation case to promote collaboration and further research into the technical challenges associated with RLVs.

This paper will first introduce the geometry of the "RFZ" vehicle and a reference trajectory based on the flight path of Falcon 9. Next, an overview of the numerical setup used for each of the cases will be presented. This is followed by results from the thrust nozzle simulations and a trim analysis at the top of glide trajectory point. Finally, a summary of results and future work is given.

2. Vehicle Design

2.1 External Aeroshape

The RFZ model is based on the SpaceX Falcon 9 and is presented in Figure 1. This vehicle was chosen because it
is the only re-usable launch vehicle which is regularly used for carrying payloads into earth orbit. The geometry was
generated using drawings and images of the Falcon 9 freely available on the internet. The vehicle is 70 metres long
with a stage 1 diameter of 3.66 metres. Some external features of the outer mold line have been omitted in the interest
of keeping the vehicle geometry as simple as possible, while still representing the complexity of a RLV. An example of
this is the substitution of the grid fins with planar fins. Grid fins require a significant amount of grid points to represent
numerically, resulting in added computational expense. In addition, they would be difficult to manufacture on a small
scale, should the model ever be tested in a wind tunnel. Hinge points for the landing legs and externally run lines are
also examples of items which have been neglected for simplicity. The launch configuration is represented by folded
fins and landing legs (RFZ-LAC), with the presence of the upper stage. The re-entry configuration is characterised by
extended planar fins and the lack of second stage (RFZ-REC), while the landing configuration features extended legs
and fins (RFZ-LDC). Each of these geometries are available for download in ref.[6].
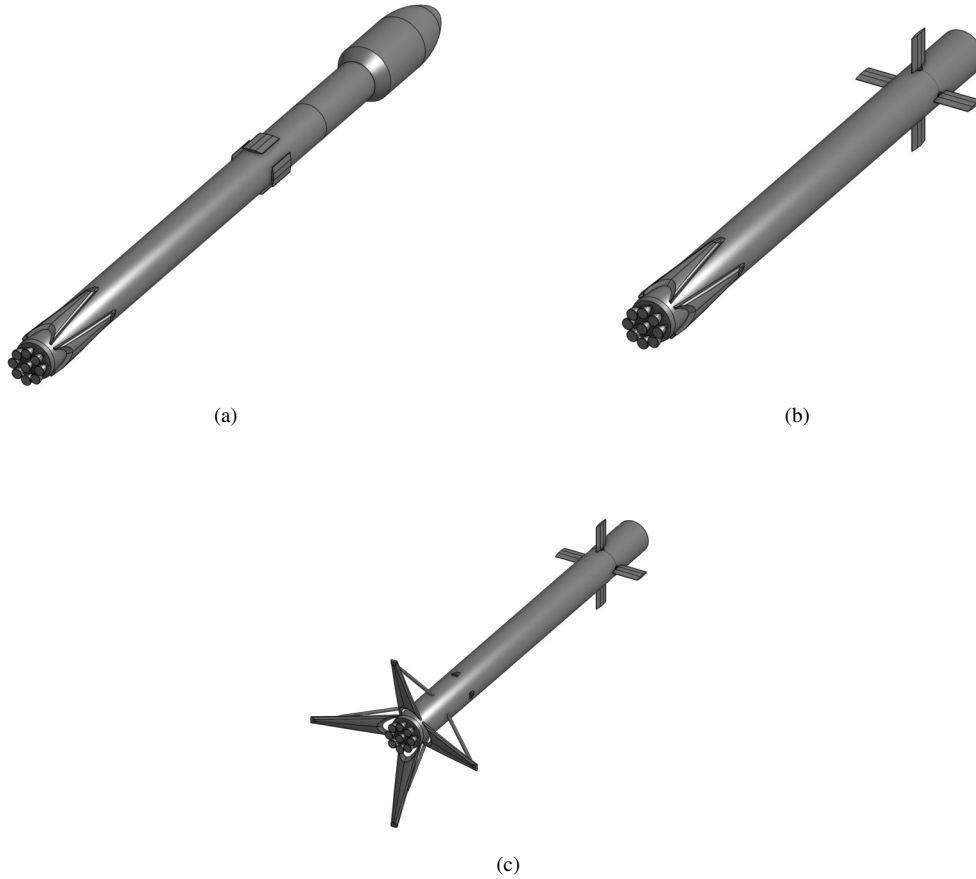

(a)

(b)

(c)

Figure 1: Images showing different views of the RFZ model (a) launch configuration (RFZ-LAC), (b) re-entry config-
uration (RFZ-REC) and (c) landing configuration (RFZ-LDC)

The planar fins feature a hexagonal cross section with a maximum thickness to chord ratio of 10%. This fin
profile was chosen over a standard diamond configuration to allow better integration of the fins to the fin holders,
which should result in easier grid generation around this area (see Figure 2). A leading and trailing edge radius of 30
mm has been used to mitigate thermal loads during re-entry and should also delay flow separation in the subsonic flow
regime at low to moderate inclination angles. The fins have a span of 3 m and and a chord length of 2 m.

The first stage peripheral nozzles are numbered one to eight clockwise starting at the positive z axis, with the
central nozzle designated as number nine (see Figure 6). The geometry for the exhaust from the gas generator has been
excluded along with any other mounting and cooling architecture. The central nozzle has been made to protrude by 0.1
metres, as is seen on the Falcon 9. A similar naming strategy has been given for the fins and landing legs.
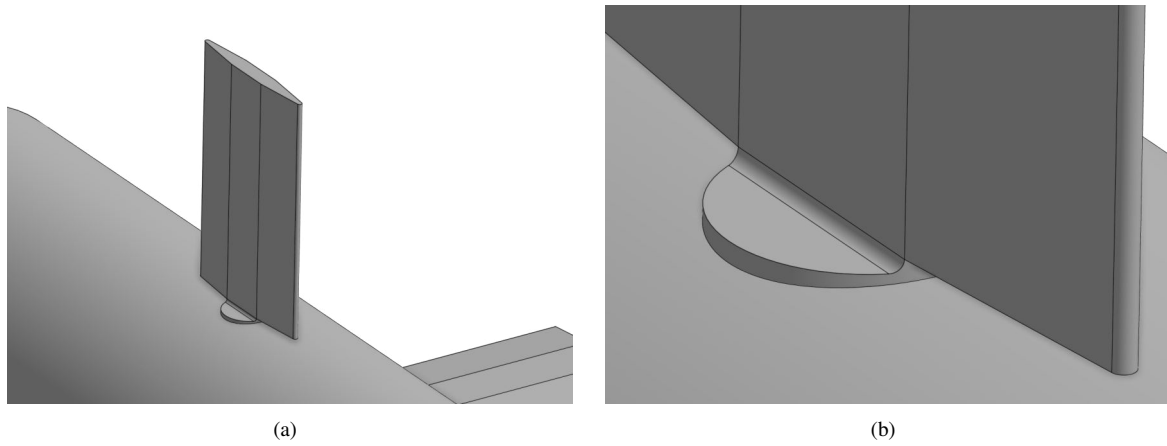
(a)

(b)

Figure 2: Images showing view of (a) fin hexagonal profile and (b) integration with fin holder
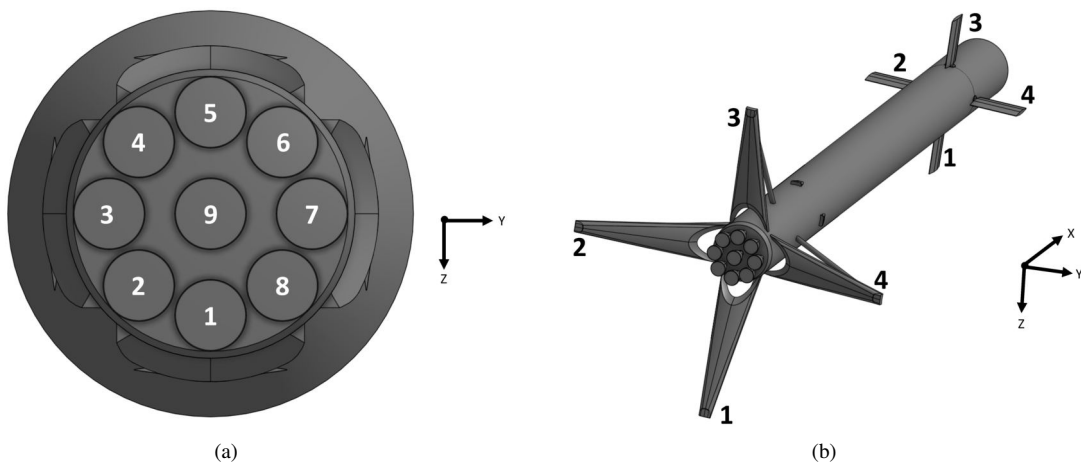

(a)

(b)

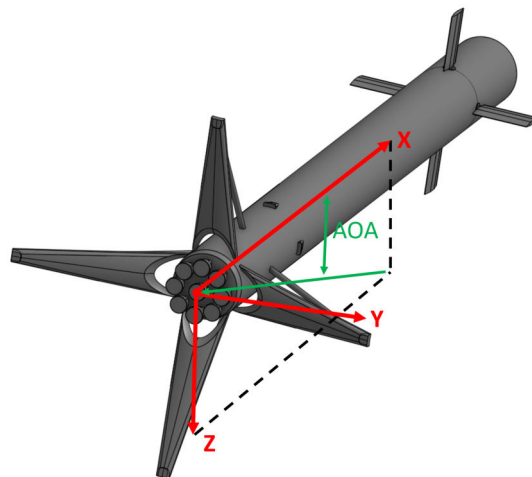Figure 3: Number designations for (a) First stage nozzles and (b) fin/landing legs

Figure 4: Fixed body axis system for RFZ vehicle

Because the CoG is constantly changing throughout the flight due to fuel consumption, a fixed point for the location of the axis system is required. The fixed body axis for these configurations is displayed above in Figure 4, where angle of attack (AoA) is treated as a combination of X and Z components as depicted. This means that for the phases of flight where the vehicle is flying backwards, the AoA will be 180 degrees for a fully symmetrical flow condition, while for forward flight this is represented by 0 degrees. The axis system is located at the exit plane of nozzle number nine, meaning that this system location is valid regardless of flight configuration.

2.2 Nozzle Contour and Engine Operating conditions

The first stage engines are largely based on the Merlin 1D+ from the SpaceX Falcon 9 launcher. The nozzle has an expansion ratio of 16:1 with a throat area of 0.042 m^2 as shown in Figure 5. A nozzle contour was generated using the method outlined by Rao in the openly available code[7] with a length ratio of 80%.
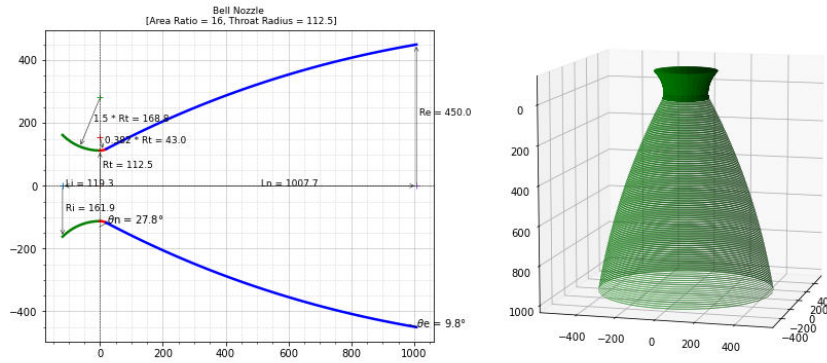

Figure 5: Stage 1 nozzle contour

The operating conditions of the nozzle are based on using kerosine as a fuel with the combustion chamber pressure set to 108 bar and an oxidiser-to-fuel ratio of 2.35 for both the first and second stage. Initial 1D investigations were made using the NASA CEA tool to determine the species and their respective mass fractions present throughout the nozzle. The mass fractions, pressure and temperature at the combustion chamber exit are used as the boundary conditions for the CFD calculations which are discussed later. The second stage nozzle is based on the vacuum variant of the Merlin 1D+ engine, with an expansion ratio of 165:1 and the same throat radius and length ratio used to define the first stage nozzle geometry. The species at both nozzle exits are summarised in Table 1 where any mass fractions smaller than 1×10^{-4} at the combustion chamber exit have been neglected.

Table 1: Overview of species mass fraction results from NASA CEA analysis for stage 1 and stage 2 engines

Species	Combustion Chamber	Throat	Exit, stage 1	Exit, stage 2
CO	0.44300	0.43407	0.37356	0.27086
CO_2	0.24605	0.26014	0.35529	0.51665
H	0.00114	0.00092	0.00001	0.00000
H_2	0.00960	0.00949	0.01240	0.01980
H_2O	0.25739	0.264	0.25871	0.36400
O	0.00366	0.00230	0.00000	0.00000
OH	0.03058	0.02309	0.00002	0.00000
O_2	0.00839	0.00554	0.0000	0.00000

2.3 Centre of Gravity

Knowledge of the CoG is critical to determine the induced pitching moment by the planar fins at different points along the trajectory. For this reason a CoG analysis will be conducted, with Figure 6 showing an overview of the different components considered. All weights and local CoGs remain static for complete trajectory aside from the LOX and RP-1 tanks on the first stage and are summarised in Table 2 for the initial conditions, i.e. with payload and fully fuelled.

Table 2: Fully loaded RFZ model with component mass and local CoGs

Component	Weight (kg)	CoG (m)	Notes
Stage 1 Shell	8000	21.0	Estimate aided by[8]
Stage 1 Fins	1520	40.3	Estimate aided by[8]
Stage 1 Engines	4230	0.452	9 engines × 470kg[9]
Stage 1 Landing Legs	2000	6.66	4 legs × 500kg[10]
Stage 1 RP1 Tank	120300	9.07	Full incl. tank weight, estimate aided by[8]
Stage 1 LOX Tank	281050	28.6	Full incl. tank weight, estimate aided by[8]
Stage 1 Interstage	400	44.8	Estimate aided by[8]
Stage 2 Shell	3300	52.2	Full tank, estimate aided by[8]
Stage 2 Engine	700	43.8	Accounts for longer nozzle extension
Stage 2 RP1 Tank	27600	49.4	Full tank, estimate aided by[8]
Stage 2 LOX Tank	64860	54.3	Full tank, estimate aided by[8]
Stage 2 Payload and Fairing	18700	62.5	1.7T fairing + 17T payload,estimate aided by[8]
Total	**532660**	**29.3**	**Approx. 41.8 % of height**

Given that the launcher will be analysed both with and without the presence of the second stage, all distance values are given relative to fixed body reference previously mentioned.
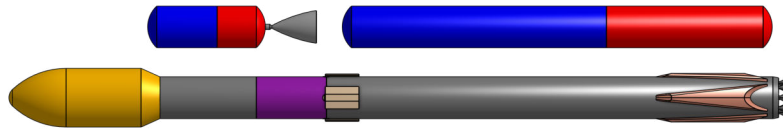

Figure 6: Overview of the various vehicle components used for CoG calculations

3. Vehicle Trajectory

Re-usable launchers of this type typically follow one of two different trajectory types. The first is a downrange landing, where the first stage is more-or-less left to follow a natural arc after stage separation and lands away from the launch site. The second is a return to landing site scenario, where following stage separation the first stage alters its trajectory by performing a boost back burn to allow it to land at a designated landing zone close to the launchpad. For both cases the vehicle will complete a re-entry burn, an aerodynamic glide and finally a landing burn. The work presented in this paper focuses on a downrange landing scenario, with an overview of the trajectory given below in Figure 7 for a low earth orbit (LEO) flight. Note that the trajectory has not been generated using any simulation tools, but rather made use of the trajectory data which is openly available from publicised Falcon 9 launches and video analysis software[11]. Given the nature of this project is to provide a platform for analysing a relevant geometry through representative flow conditions, this approach is considered valid. In addition, trajectory simulations would require simplifications and assumptions, which may not result in a more accurate trajectory than that taken from Falcon 9 webcasts.

A summary of the key events along the trajectory is given below in Table 3 alongside the geometry relevant to the flight phase. At approximately 70 km altitude stage separation occurs and this is set as the end of the launch phase. An important consideration is that the apogee of the first stage is at an altitude of around 130 km. At approximately 90 km the assumption of continuum fails to be valid as the Knudsen number exceeds 0.01 and as a result, all CFD work will be conducted below this limit.

Table 3: Summary of key flight events

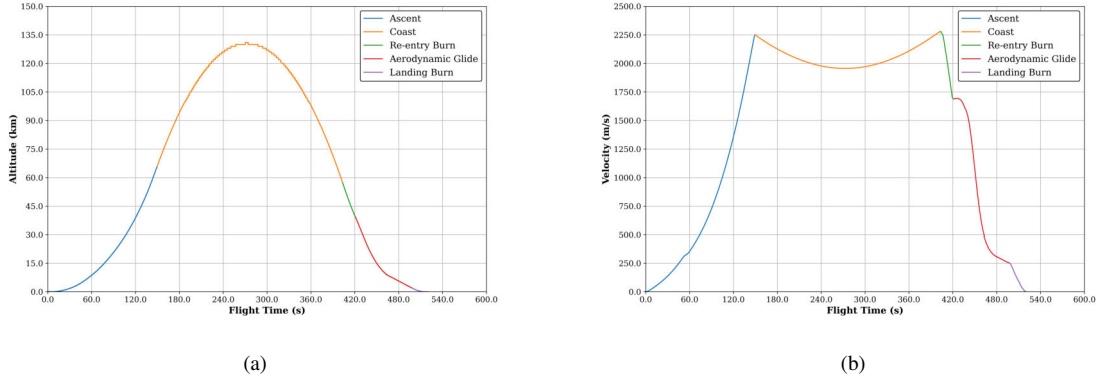| Time (s)	Event	Geometry
150	MECO	RFZ-LAC
403	Re-entry burn start	RFZ-REC
421	Re-entry Burn end	RFZ-REC
498	Landing Burn Start	RFZ-REC
521	Landing Burn End	RFZ-LDC

(a)

(b)

Figure 7: Plots showing the full LEO trajectory for the first stage with key events for (a) altitude and (b) velocity

4. Numerical Setup

The Tau code is a second order finite-volume solver for the Euler and Navier-Stokes equations which includes a comprehensive range of RANS-based or scale resolving turbulence models. It uses unstructured computational grids to facilitate the analysis of complex geometries and is highly optimized for the application on massively parallel HPC systems. Tau has been successfully applied to a wide range of sub-to-hypersonic flow problems, both in scientific and industrial applications, including the analysis of re-usable launcher configurations[12–15]. The baseline set of numerical models which have been applied for the present investigations provides accurate and robust treatment for the top of glide conditions. The calculation of the inviscid fluxes in the finite volume framework is based on the application of the AUSMDV flux vector splitting scheme together with MUSCL gradient reconstruction to achieve second order spatial accuracy. Viscous fluxes are treated with a low-dissipation central discretization scheme.

For this paper, turbulence was modelled with a Spalart-Allmaras one-equation RANS model. The single equation turbulence model provides a good compromise between numerical efficiency and accuracy and is particularly applicable to flows with strong compression shocks. This model completely resolves the structure of the turbulent boundary layer including the laminar sub-layer. Thus, an adequate setup of the numerical grid is required which is achieved by using prismatic sub-layers close to the wall with a first dimensionless wall spacing of y^+ in the order of one and a wall normal stretching ratio of grid cells of less than 1.3. The wall temperature was set to 300K and heat flux was assumed to be isothermal.

Simulations of the external flow during the ascent, re-entry burn or landing burn require an accurate representation of the nozzle exhaust. It is assumed that the nozzle outflow conditions for all engines are equal and are independent of the external conditions, i.e. no flow separation in the nozzle due to high external pressures. To model combustion the chemical non-equilibrium solver within Tau was used considering the 8 species presented in Table 1. A single nozzle computation can be completed using a 2D axisymmetric grid. This allows independent analysis of the flow in the nozzle and reduces the overall point count in the external flow grid. The conditions at the nozzle exit plane are easily interpolated onto the external flow grid where a dirichlet boundary condition is used. The grid used for the external flow simulations is presented below in Figure 8. The grid uses a spherical domain with approximately 50 rocket lengths upstream and downstream of the vehicle centrepoint. This means that the grid can be used for both hyper/supersonic and subsonic cases, with the only modifications required being to the first cell height to ensure compliance with a y^+ equal to unity. For cases which are symmetrical about the X-Z and Y-Z planes, a quarter domain is used, while for cases with only symmetry in the Y-Z plane, a half grid is used. The investigations presented here are considered as preliminary studies and thus a high density grid is not required. For this reason the quarter configurations contain approximately 2.4 million points, with the half grids containing double this figure.

External flow simulations have been conducted at one trajectory point to first understand the flow field around the vehicle and make preliminary heat flux assessments. Secondly, the pitching moments are evaluated to understand the effectiveness of the planar fins at trimming the vehicle. Trajectory point one is at the start of the aerodynamic glide phase, i.e. after engine shutdown from the re-entry burn. A summary of the test points with a description is provided in the table below.
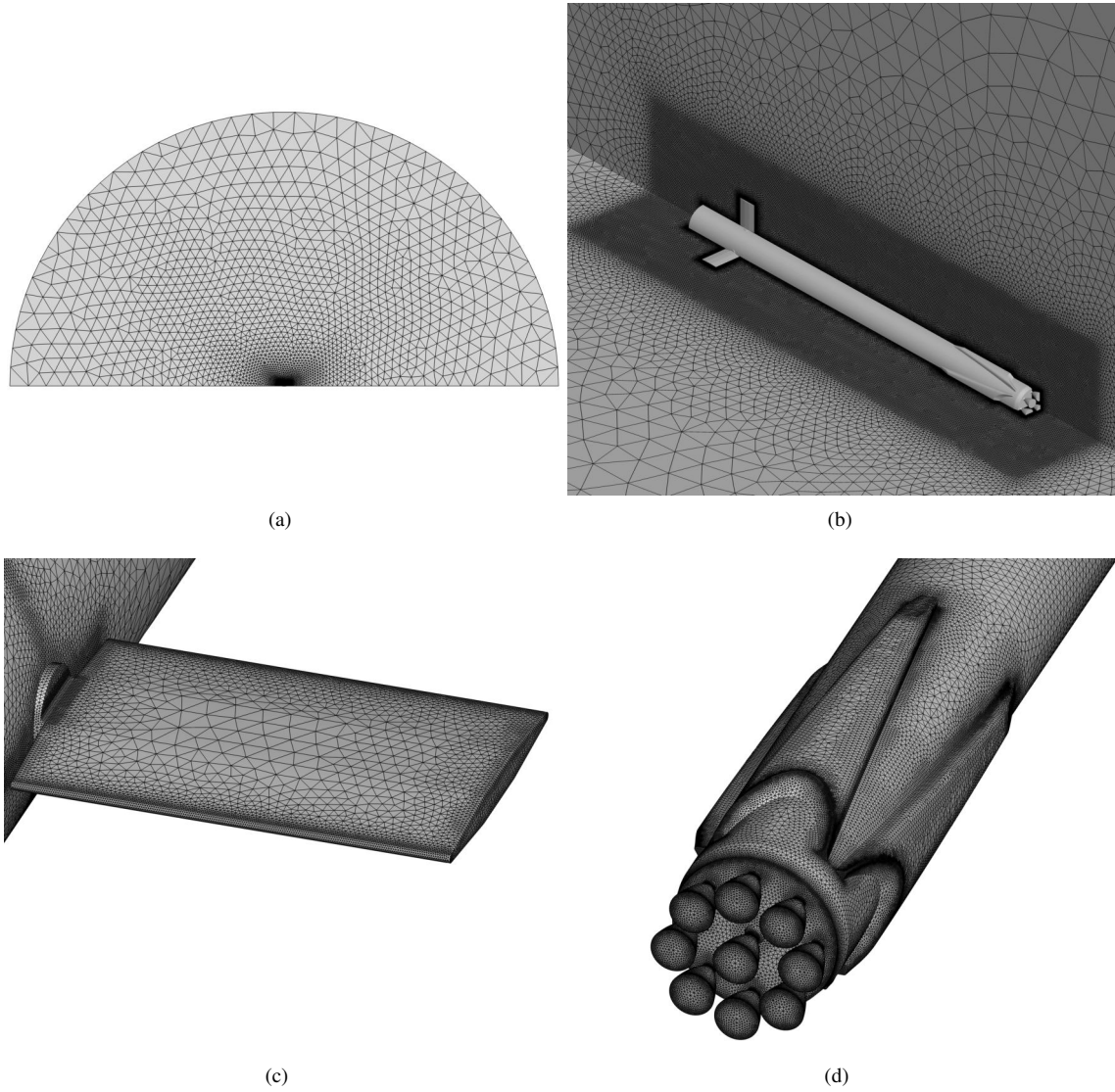
(a)

(b)

(c)

(d)

Figure 8: Images showing different views of the RFZ model grid (a) farfield, (b) refinement region, (c) base and (d) fins

Table 4: Test matrix

No.	V_∞ (m/s)	P_∞ (Pa)	T_∞ (K)	AoA (deg)	Plume (on/off)	Fin Angle (deg)	CoG (m)
1	1689.7	368.1	245.4	180	off	0	15.26
2	1689.7	368.1	245.4	185	off	0	15.26
3	1689.7	368.1	245.4	190	off	0	15.26
4	1689.7	368.1	245.4	180	off	10	15.26
5	1689.7	368.1	245.4	185	off	10	15.26
6	1689.7	368.1	245.4	190	off	10	15.26

5. Results and Discussion

5.1 2D Internal Nozzle Flow and CoG

Post processed images of the nozzle calculations for the internal flow of the first stage engines are presented below in Figure 9. The pattern of the Mach contours suggest the presence of an internal shock, which is typical for this type of nozzle contour. Evaluating the mass flow through the engine, a value of approximately 250.8 kg/s was obtained from both the CEA tool and Tau computations. An additional consideration for the engine mass flow is the gas generator. This is not relevant to the external or internal flow calculation, as no gas generators are physically modelled. It is

instead required for the fuel consumption estimates, which in turn impact the variation of the CoG as fuel is being burned. For this reason a value of 5% of the total engine mass flow is assumed to be used by the gas generator and is added to the Tau mass flow result, giving a total mass flow rate per engine of approximately 263.3 kg/s.

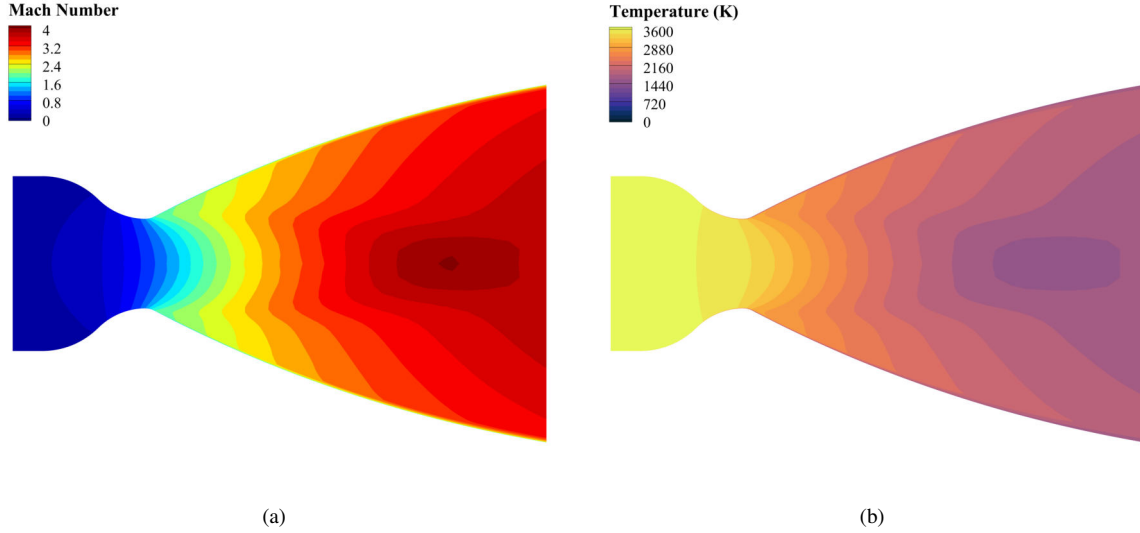(a)   (b)

Figure 9: Internal flow results for the first stage nozzle showing distributions of (a) Mach number and (b) temperature

Figure 11(b) presents the outcome of the CoG studies. The CoG shift has been calculated by considering the drain rate of the stage 1 RP-1 and LOX tanks. This is taken as a function of the number of active engines, throttle setting and the combined nozzle and gas generator flow rate. For this simple analysis, the engines are assumed to be operating at 100% throttle, except for 10 seconds leading up to the point of maximum dynamic pressure. Here the fuel flow is reduced to 80%. Given the shape of the fuel tanks, the the mass of fuel in the tanks can be simply represented by a cylinder with a CoG at exactly half its height. The fuel is assumed to drain downwards and no deviation in the cylindrical shape due to factors like inclination angle of the vehicle is accounted for. Based on these assumptions, the height of the cylinder reduces as fuel is burned, which in turn lowers the CoG.

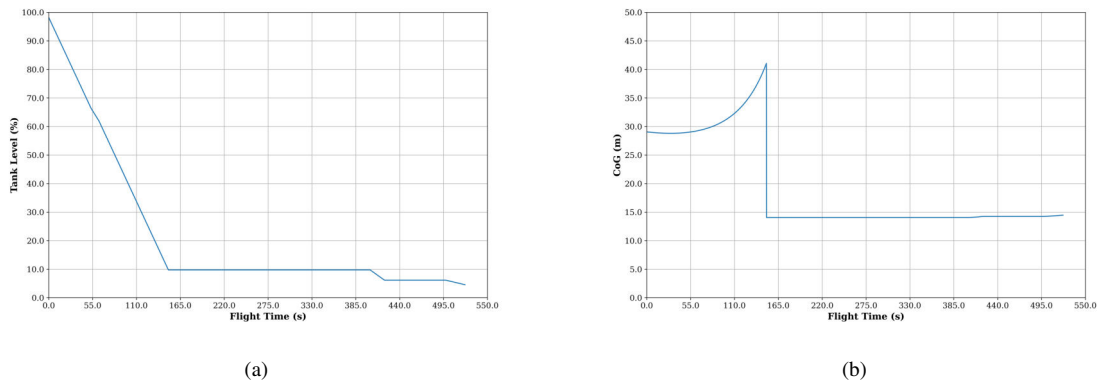(a)   (b)

Figure 10: Results from the CoG calculation showing (a) percent fuel remaining and (b) CoG position

Initially the CoG of the launcher is dominated by the stage 1 fuel mass with a local CoG shifting downwards. As the fuel continues to drain, the higher mass of the second stage begins to dominate the CoG calculation, resulting in a forward shift. The large drop in CoG occurs at stage separation, where the second stage no longer attached to the vehicle. The influence of subsequent burns is able to be observed, alongside the points of static CoG, where the vehicle is gliding. Figure 11(a) illustrates that approximately 4% fuel is remaining in the tanks at touchdown.

5.2 Flowfield and Heating

Figure 11 presents the symmetry plane density gradient magnitudes for both 0 and 10 degree AoA cases. Given the nozzles are not operational, a detached bow shock forms around the nozzles, with a shock stand off distance of

approximately half of the nozzle extension length at 0 degrees AoA. Asymmetry in the shock pattern is introduced as the vehicle pitches upwards and additional high density gradients appear at the tip of fin 1 and the windward rim of the interstage bay. Here the local Mach numbers are higher than those on the leeward side, leading to stronger compression and expansions of the flow.

(a)   (b)
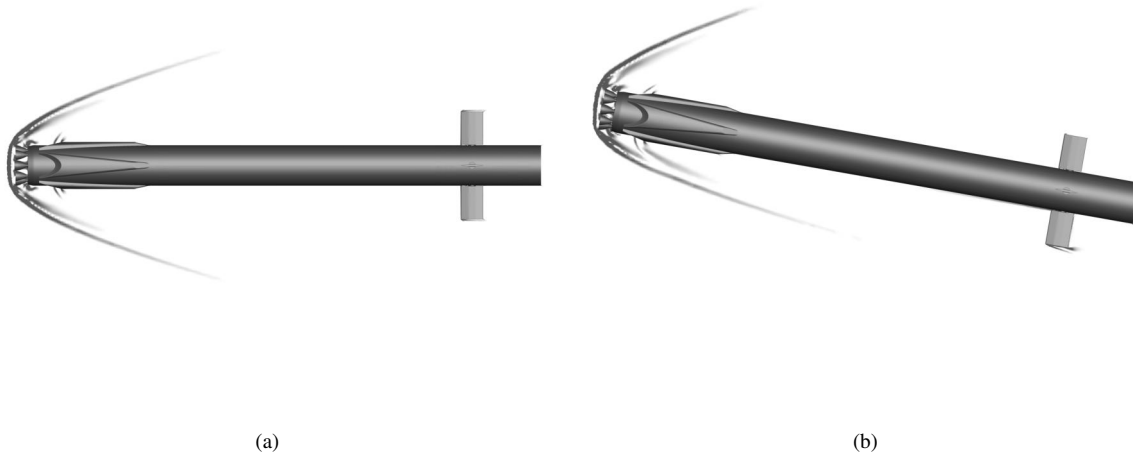
Figure 11: Symmetry plane density gradient magnitude for (a) 0 degree AoA and (b) 10 degree AoA

Figure 12 presents a comparison of fin leading edge heat flux for 0 and 10 degree AoA cases. For the 10 degree case, fin number 1 has a higher exposure to the incoming flow and experiences the largest heat fluxes. On the contrary, fin 4 which is shielded by the body of the vehicle sees the lowest heat flux. The symmetric case at 0 degrees AoA sees low to moderate values, highlighting the influence of AoA on the asymmetric heating distribution between the fins.
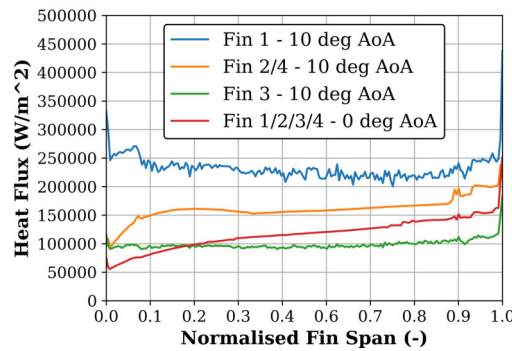

Figure 12: Comparison of fin leading edge heat flux for 0 and 10 degree AoA cases

Post processed images of the baseplate for both the cases at 0 and 10 degrees AoA are presented in Figure 13. For the 0 degree case, the symmetry of the pressure coefficient and heat flux patterns are clear and expected. The regions of high heat flux are located at regions where the peripheral nozzles intersect with the baseplate facing towards nozzle 9. This is where flow directly impinges the baseplate and either reverses towards nozzle 9 or wraps around the nozzle before separating and creating a small wake region. This can be clearly seen in 13 (b). The point of impingement directly correlates to the highest region of heat flux, while the wake region behind the base of the peripheral nozzles and location where flow reverses experiences lower heat flux. In addition, zones of low heat flux extending from the centre of the baseplate between the peripheral nozzles can be seen. This is due to the flow between nozzles meeting and separating, causing local regions of flow recirculation. Similar mechanisms are at play for the 10 degree case, however the asymmetry introduced by the oncoming flow results in a shift in heat flux and pressure coefficient patterns. Figure 14 further illustrates the degree of flow reversal which can be seen in the baseplate skin friction lines in 13 (b). The mechanism behind the regions of low heat flux seen in 13 (a) can be visually deduced by analysing the separated flow originating from nozzle 9. This also results in lower heat flux at nozzle 1 and 5 when compared to 0 degrees AoA.
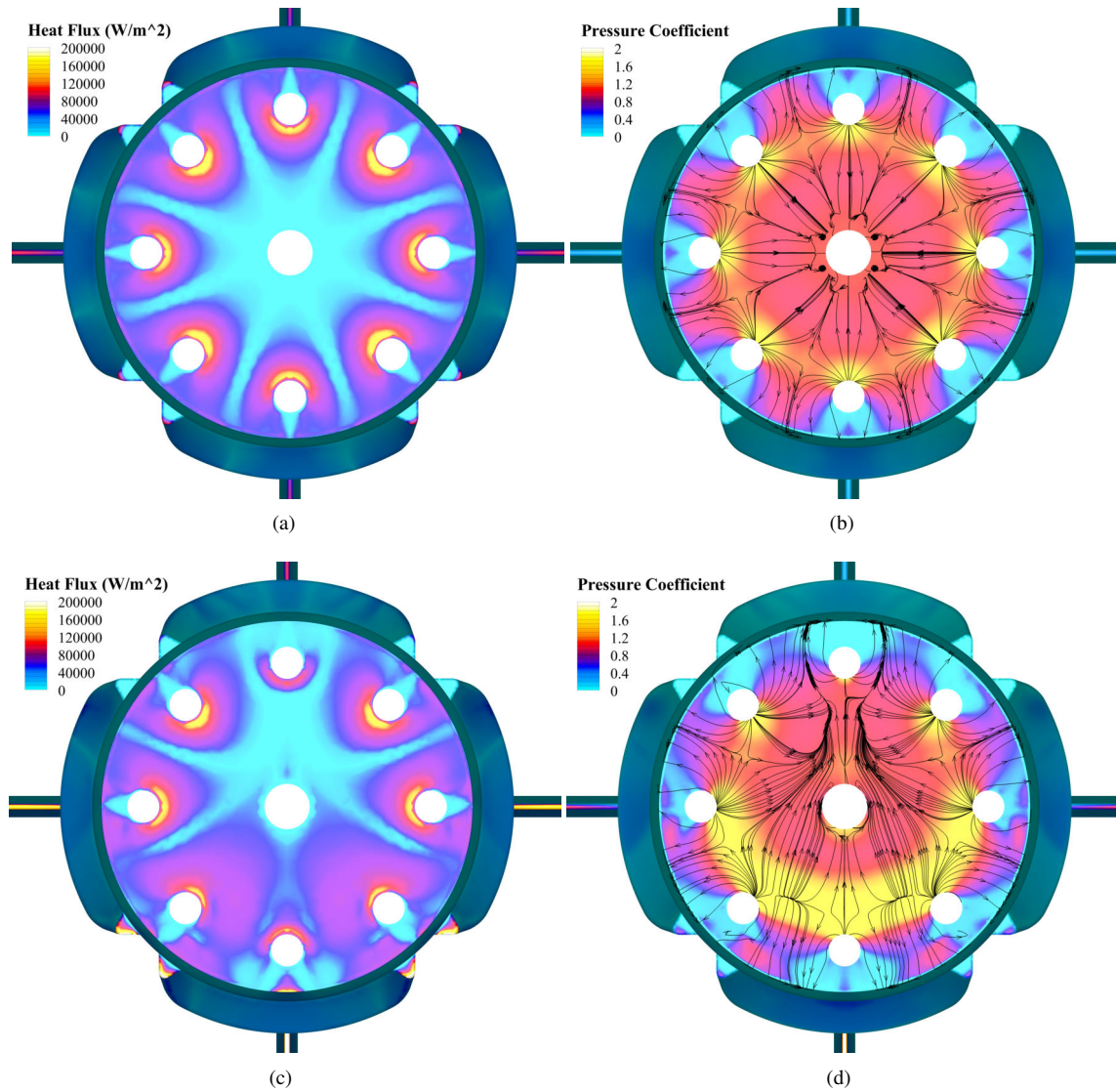
Figure 13: Images from start of glide for (a) baseplate heatflux at 0 degee AoA, (b) baseplate pressure coefficient at 0 degee AoA, (c) baseplate heatflux at 10 degee AoA and (d) baseplate pressure coefficient at 10 degee AoA
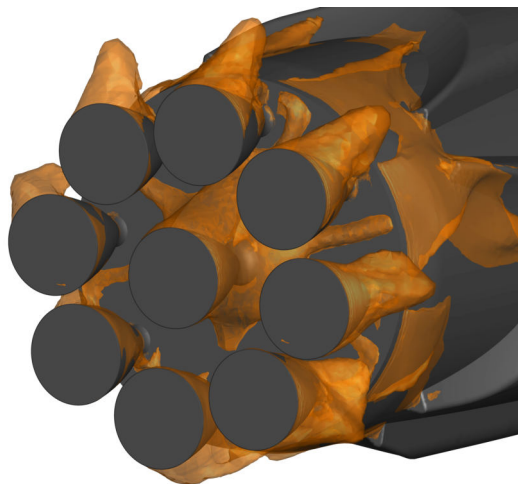

Figure 14: Isosurface showing regions of reversed flow for the 10 degrees AoA case

5.3 Aerodynamic Coefficients and Trim

A trim analysis using the tabulated aerodynamic coefficients in Table 5 at the top of the aerodynamic glide shows that with 10 degrees planar fin deflection angle, the vehicle can be trimmed at approximately 186 degrees AoA. This is an estimate based on three different AoA points, which does not completely capture the non-linear behaviour of the pitching moment coefficient which appears to be present. Further investigation using higher AoA resolution will result in a more accurate trim prediction. The offset in pitching moment curves achieved by the deflection of the planar fin can be visualised in Figure 15.

Table 5: Aerodynamic coefficient results for start of glide

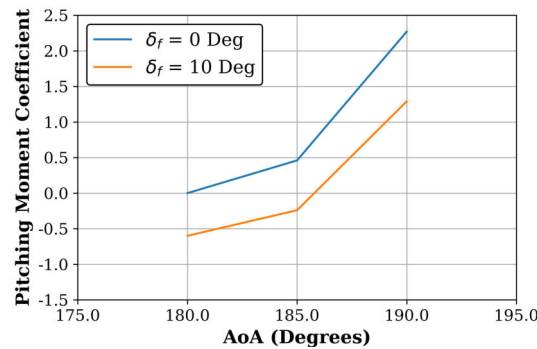| AOA (deg)	PFD (deg)	C_X	C_Z	C_L	C_D	C_m
180	0	1.65	0.00	0.00	1.65	0.00
170	0	1.69	0.90	0.59	1.81	-2.18
180	10	1.66	0.08	0.08	1.66	-0.62
185	10	1.67	-0.17	-0.03	1.68	-0.21
190	10	1.68	-0.76	-0.46	1.79	1.44

Figure 15: Pitching moment vs AoA for fin deflections of 0 and 10 degrees

6. Conclusions and Future Work

This paper has introduced a standard model to be used for numerical or experimental investigations relating to reusable launch vehicles. The geometry and all results are publicly available for members of the research community to access. The vehicle has three configurations which are representative of launch, re-entry and landing phases of flight. Results from initial investigations relating to the internal flow of first stage nozzles, as well as external flow at the start of the aerodynamic glide phase have been presented. A trim analysis was also conducted using data from a GoG analysis, which showed the ability to trim the vehicle at 186 degrees AoA with 10 degrees of fin deflection angle. Initial heating estimates have been made for a cold wall condition of 300K, which highlighted the asymmetric heat loads on both the baseplate and fins due to angle of attack. Future work includes a range of sensitivity analyses for grid densities, turbulence models and chemistry models. This will be followed by the development of a comprehensive aerothermal database which will allow heat load estimates over the entire trajectory. Other possibilities include work on yet to be determined test cases, including but not limited to, surface heating through retro-propulsion and aerodynamic glide phases, plume-plume and plume-structure interactions, as well as vehicle stability and control, with the goal of collaborations between multiple research institutions to be able to compare and contrast results from various codes.

References

[1] North Atlantic Treaty Organization. Advisory Group for Aeronautical Research and Development. Wind tunnel calibration models - agard specification 2. Technical report, NATO, 1958.

[2] R.D. Galway and M. Mokry. Wind tunnel tests of onera aircraft models. Technical report, National Aeronautical Establishment, 1977.

[3] M. Beyers and X. Huang. Subsonic Aerodynamic Coefficients of the SDM at Angles of Attack up to 90°. Technical report, NRC, Ottowa, Canada, 1990.

[4] M. B. Rivers, J. Quest, and R. Rudnik. Comparison of the nasa common research model european transonic wind tunnel test data to nasa test data (invited). In *AIAA SciTech Forum*, Kissimmee, Florida, Jan 2015.

[5] T. Bykerk, N.F. Giannelis, and G.A. Vio. Static aerodynamic analysis of a generic fifth generation fighter aircraft. In *AIAA SCITECH 2022 Forum*, 2021.

[6] T. Bykerk. Rfz data repository, 2023. `https://zenodo.org/communities/rfz-model/?page=1&size=20`.

[7] Ravi4Ram. Bell nozzle, 2023. `https://github.com/ravi4ram/Bell-Nozzle`.

[8] Wikipedia. Falcon 9 full thrust, 2023. `https://en.wikipedia.org/wiki/Falcon_9_Full_Thrust#Rocket_specificationse`.

[9] Thomas Mueller. Is spacex's merlin 1d's thrust-to-weight ratio of 150+ believable?, 2017. `https://www.quora.com/Is-SpaceXs-Merlin-1Ds-thrust-to-weight-ratio-of-150+-believable`.

[10] Elon Musk. How much do the landing legs on spacex f9 rockets weight?, 2013. `https://www.quora.com/How-much-do-the-landing-legs-on-SpaceX-F9-rockets-weigh`.

[11] shahar603. Spacextract, 2023. `https://github.com/shahar603/SpaceXtract`.

[12] T. Ecker, S. Karl, E. Dumont, S. Stappert, and D. Krause. Numerical study on the thermal loads during a supersonic rocket retropropulsion maneuver. *Journal of Spacecraft and Rockets*, 57(1), 2020.

[13] T. Bykerk, D. Kirchheck, and S. Karl. Reconstruction of wind tunnel tests using cfd for a reusable first stage during rocket retro-propulsion. In *International Conference on Flight Vehicles, 9th European Conference for Aeronautics and Space Sciences (EUCASS)*, Lille, France, July 2022.

[14] T. Bykerk, D. Kirchheck, and S. Karl. Condensation modelling of expanding cold gas jets during hypersonic retro-propulsion manoeuvres within the retpro project. In *23rd Australasian Fluid Mechanics Conference (AFMC)*, Sydney, Australia, December 2022.

[15] T. Bykerk and S. Karl. Preparatory cfd studies for subsonic analyses of a reusable first stage launcher during landing within the retpro project. In *International Conference on Flight Vehicles, 9th European Conference for Aeronautics and Space Sciences (EUCASS)*, Lausanne, Switzerland, July 2023.